Bayesian Inference of Hemodynamic Changes in Functional Arterial Spin Labeling Data

Mark W. Woolrich,[1,*] Peter Chiarelli,[1] Daniel Gallichan,[1] Joanna Perthen,[2] and Thomas T. Liu[2]

The study of brain function using MRI relies on acquisition techniques that are sensitive to different aspects of the hemodynamic response contiguous to areas of neuronal activity. For this purpose different contrasts such as arterial spin labeling (ASL) and blood oxygenation level dependent (BOLD) functional MRI techniques have been developed to investigate cerebral blood flow (CBF) and blood oxygenation, respectively. Analysis of such data typically proceeds by separate, linear modeling of the appropriate CBF or BOLD time courses. In this work an approach is developed that provides simultaneous inference on hemodynamic changes via a nonlinear physiological model of ASL data acquired at multiple echo times. Importantly, this includes a significant contribution by changes in the static magnetization, *M*, to the ASL signal. Inference is carried out in a Bayesian framework. This is able to extract, from dual-echo ASL data, probabilistic estimates of percentage changes of CBF, R_2^*, and the static magnetization, *M*. This approach provides increased sensitivity in inferring CBF changes and reduced contamination in inferring BOLD changes when compared with general linear model approaches on single-echo ASL data. We also consider how the static magnetization, *M*, might be related to changes in CBV by assuming the same mechanism for water exchange as in vascular space occupancy. Magn Reson Med 56:891–906, 2006. © 2006 Wiley-Liss, Inc.

Key words: ASL; FMRI; CBF; Bayes; BOLD

Functional magnetic resonance imaging (FMRI) techniques can be used for noninvasive spatial mapping of neural activity in the healthy and pathological brain. Such techniques are sensitive to the effect that the neural activity has on hemodynamic changes in the vasculature adjacent to the activity. Hence, subjects can be scanned while performing cognitive tasks, spatially localizing areas of the brain in which the task-induced neural activity causes measurable changes in the hemodynamics.

The most popular of the FMRI techniques is blood oxygenation level dependent (BOLD) sensitive FMRI (BOLD-FMRI) (1,2). This is predominantly sensitive to changes in the oxygenation of the blood that occur in regions of the vasculature near neural activity. The hemodynamic changes that result in the BOLD effect are due to a combination of physiological parameters, for example, CMRO2 (cerebral metabolic rate of oxygen [consumption]), CBF (cerebral blood flow), and CBV (cerebral blood volume) (3,4). FMRI techniques such as arterial spin labeling (ASL) (5,6), and more recently vascular space occupancy (VASO) (7), have also been developed for providing windows on CBF and CBV respectively, without the need for exogenous contrast agents.

One of the main reasons why BOLD-FMRI is so widely used is its high contrast-to-noise ratio (CNR) relative to ASL-FMRI and VASO-FMRI (7,8). However, there are still a number of reasons why it would be advantageous to consider these other techniques as well. First, particularly at lower field strengths (1.5–3 T), ASL-FMRI and VASO-FMRI can potentially provide measurements of hemodynamic changes more directly related to the capillary beds contiguous to the sites of neuronal activity (7–9). Second, it is difficult to assess the performance of models that relate BOLD signal all the way back to a stimulation task. Techniques such as ASL and VASO can be used for providing valuable intermediate information (10). Third, ASL-FMRI and VASO-FMRI individually provide direct, quantitative measurements of physiologically meaningful parameters (CBF and CBV, respectively). For example, it has been well demonstrated that by using calibration via hypercapnia, BOLD-FMRI and ASL-FMRI can be combined to estimate steady-state neural activity induced changes in CMRO2 (11).

Most current acquisition techniques are aimed at giving separate, pure information about CBF, CBV, or BOLD. For example, measurements of ASL and BOLD can be made by interleaving ASL and BOLD acquisition (11). Single-shot multiecho data have also been used previously to obtain increased BOLD sensitivity and quantitative T_2^* mapping (12). This provides distinction of T_2^* effects from other factors, such as inflow and hardware instabilities. Dual-echo ASL data have also been used to separate T_2^* effects from CBF effects in ASL images (13–15).

However, analysis of such data typically proceeds by separate, linear modeling of the appropriate CBF or BOLD time courses (11,16,17). In this work, we instead propose an approach that provides inference on the relevant functional changes in the blood via a physiological model of ASL data acquired at multiple echo times. This can be achieved with a simple nonlinear model of the physiology, which describes the observed signal in terms of functional changes in CBF and T_2^*, and static magnetization, M (the static magnetization consists of blood and tissue that remains in a voxel from the time of the blood tagging to the image acquisition). This is then inferred upon using a Bayesian framework. We demonstrate this approach on single-shot dual-echo ASL data and on ASL data interleaved at two different echo times.

We show that we can extract, from dual-echo ASL data, probabilistic estimates of percentage changes of not only CBF and T_2^*, but also the static magnetization, M. We show

[1]University of Oxford, Centre for Functional MRI of the Brain, John Radcliffe Hospital, Oxford, United Kingdom.

[2]UCSD Center for Functional MRI, University of California at San Diego, San Diego, California.

*Correspondence to: Mark Woolrich. E-mail: woolrich@fmrib.ox.ac.uk

Received 1 February 2006; revised 28 June 2006; accepted 6 July 2006.

DOI 10.1002/mrm.21039

Published online 8 September 2006 in Wiley InterScience (www.interscience.wiley.com).

that extracting percentage CBF using this approach is more sensitive than standard approaches of extracting it from general linear models (GLM) of ASL data at a single echo time (16,17). We also demonstrate the contribution of the static compartment, M, contribution to the ASL signal, which has not (to our knowledge) been previously reported. Taking the contribution of this component into account provides reduced contamination in inferring BOLD changes when compared with GLM approaches on single-echo ASL data. The nonlinear ASL signal model described in this paper incorporates these different hemodynamic components, allowing them to be inferred from dual-echo ASL data with more accuracy and sensitivity than current GLM approaches on single-echo ASL data. We also consider how the static magnetization, M, can be related to changes in CBV assuming a similar physiological mechanism to VASO. This method has the potential to allow for a range of complementary, quantitative information to be efficiently gathered from functional MRI brain studies.

THEORY

ASL Model

The physiological model we will use is based in part on the ASL signal processing model introduced by Liu et al. (18). The ASL signal, p_n, where $n = 1 \ldots N$ indexes the ASL scan number in a series of N ASL scans, is assumed to exhibit a simple exponential dependence on the echo time, TE, and the transverse relaxation rate (R_2^*),

$$p_n = S_n e^{-\mathrm{TE} r_0 (1 + r_n/100)}, \quad [1]$$

where r_0 is the baseline R_2^*, r_n is the percentage change in R_2^*, and S_n is the magnetization in a voxel. The magnetization in a voxel, S_n, is modeled as two compartments consisting of the magnetization due to tagged (or untagged) arterial blood that flows into the observed voxel, S_n^b, and of the magnetization that remains static in the voxel, S_n^s,

$$S_n = S_n^s + S_n^b. \quad [2]$$

Arterial Blood Flow Compartment

In the arterial blood flow compartment, the term S_n^b represents the magnetization that is delivered into the voxel in the blood. Note that because we are looking for a full model of the observed data, we are not just modeling magnetization *differences* between tag and control. Instead, we need to model the magnetization arriving into the voxel in the blood under both the tag and the control conditions. This requires us to take into account the T_1 recovery of the magnetization throughout the sequence. In this work we use a specific model of this magnetization recovery by assuming that the ASL data is from a QUIPSS II sequence (9). However, the model could be easily adapted for other sequences.

Figure 1 shows the T_1 recovery for the different types of arterial blood, which we assume to have been delivered to an imaged voxel in a QUIPSS II sequence. This includes tagged and untagged blood and also saturated blood, which has experienced the QUIPSS II saturation pulse applied to the tagging region at time TI_1.

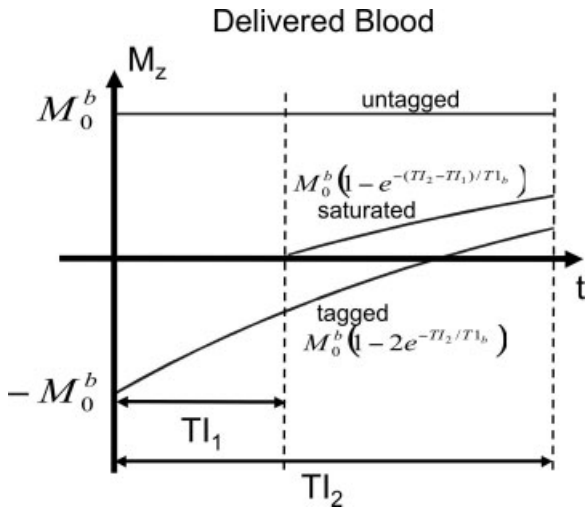

FIG. 1. T_1 recovery for the different types of arterial blood that we assume to have been delivered to an imaged voxel in a QUIPSS II sequence. This includes tagged and untagged blood and also saturated blood, which has experienced the QUIPSS II saturation pulse applied to the tagging region at time TI_1. TI_2 is the time between the inversion and image acquisition, and TI_1 is the time between the inversion and saturation pulse in the tag region.

The QUIPSS II saturation pulse is designed to produce a tagged bolus of sharply defined time width TI_1, which leaves the tagging region and is assumed to have entered the imaging region before image acquisition (9). This assumes that TI_1 is less than the original bolus width generated by the inversion in the tagging region.

In Buxton (19) and Wong (9) exchange between the static compartment and the delivered blood, and clearance of this delivered blood due to outflow, are modeled in the factor q. As discussed in Buxton (19) and Wong (9), at the inversion times used in QUIPSS II these effects are considered small, resulting in a value for the factor q close to unity. In this work we assume $q = 1$, i.e., that there is no exchange between the static compartment and the delivered blood and no clearance of the delivered blood due to outflow. We discuss this assumption under Model Validity the Discussion.

Using these assumptions we can say that the blood arriving at the imaging region at time t after the tag is

$$\begin{aligned} 0 < t < \delta t &: \text{untagged blood} \\ \delta t < t < \delta t + \mathrm{TI}_1 &: \text{tagged blood/untagged blood} \\ \delta t + \mathrm{TI}_1 < t < \mathrm{TI}_2 &: \text{saturated blood}, \end{aligned} \quad [3]$$

where δt, the transit delay, is the time between the application of the tag and the first arrival of blood in the imaging region. Of the tagged blood/untagged blood arriving in a voxel during the period $\delta t < t < \delta t + \mathrm{TI}_1$, we assume that under the ASL control condition all of it is untagged, and under the tag condition α of it is tagged and $1 - \alpha$ of it is untagged (where α is the inversion efficiency of our tagging). The total amount of arterial blood that has arrived in a voxel at time $t = \mathrm{TI}_2$ since tagging will be CBF $\times$ TI_2.

We can now combine this with the recovery curves for tagged, untagged, and saturated blood in Fig. 1 to give the

magnetization that has arrived in a voxel at time $t = \mathrm{TI}_2$ under the control condition as

$$\rho_0^b q_0(1 + q_n/100)\big(\delta t + \mathrm{TI}_1 + (\mathrm{TI}_2 - \mathrm{TI}_1 - \delta t) \times (1 - e^{-(\mathrm{TI}_2 - \mathrm{TI}_1)/\mathrm{T}_{1b}})\big) \quad [4]$$

and under the tag condition as

$$\rho_0^b q_0(1 + q_n/100)\big(\delta t + \mathrm{TI}_1(1 - 2\alpha e^{-\mathrm{TI}_2/T_{1b}}) + (\mathrm{TI}_2 - \mathrm{TI}_1 - \delta t)(1 - e^{-(\mathrm{TI}_2 - \mathrm{TI}_1)/T_{1b}})\big), \quad [5]$$

where ρ_0^b is the relaxed magnetization per unit volume of arterial blood, q_0 is the baseline CBF, q_n is the percentage change in CBF, and T_{1b} is the T_1 of the arterial blood. This gives the magnetization present in the arterial blood compartment at time $t = \mathrm{TI}_2$ as approximately

$$S_n^b = \rho_0^b q_0(1 + q_n/100)\mathrm{TI}_1(R\rho_n + (1 - R)) + \rho_0^b q_0(1 + q_n/100) \times \big((\mathrm{TI}_2 - \mathrm{TI}_1 - \delta t)(1 - e^{-(\mathrm{TI}_2 - \mathrm{TI}_1)/T_{1b}}) + \delta t\big), \quad [6]$$

where $R = \alpha e^{-\mathrm{TI}_2/T_{1b}}$. The alternating tag and control conditions are represented by the term ρ_n, which is 1 for control and -1 for tag. The first term in Eq. [6] is equivalent to that found in Liu et al. (18). However, the second term extends the model of Liu et al. (18) to handle saturated blood T_1 recovery and transit time delays.

Static Compartment

This compartment models the static components. This is defined as any magnetization that is in the voxel at the time of the tagging pulse and is still within the voxel at the time of image acquistion. At this stage we do not make any further assumptions about the form of the magnetization.

Crucially, we are assuming that the static magnetization per voxel varies with time:

$$S_n^s = M_0(1 + M_n/100), \quad [7]$$

where M_0 is the baseline static compartment signal and M_n is the percentage change in the static compartment signal. Note that even though we assume the use of a presaturation pulse in the image plane at time TI_2 prior to image acquisition, we do not explicitly model any longitudinal relaxation. Instead, this will be absorbed into the M_0 term.

Under Inferring CBV Changes we will consider what might constitute the static compartment magnetization. In particular, we will consider whether it is possible to separate the contributions to the static compartment of tissue and blood, including effects of longitudinal relaxation, to relate M_n to changes in CBV in the same manner as VASO (7).

Percentage R_2^*, CBF and M Temporal Models

We now must specify what we assume about the time series of the percentage change in R_2^*, CBF, and M in response to known experimental stimuli in a functional experiment. We take an approach commonly used in standard BOLD-FMRI analysis by using basis functions to provide flexibility in fitting the response shape within a simple mathematical framework (20).

If we have $j = 1 \ldots J$ basis functions to model the response, then for CBF we have

$$q_n = \sum_{j=1}^{J} Q_j x_{jn}, \quad [8]$$

where Q_j is the CBF parameter for the *jth* basis function, $\boldsymbol{x_j}$. The choice of basis set will be determined by the nature and extent of the flexibility that we want to allow in the response shapes. It might be a set of stimulus convolved basis functions or a set of basis functions that span the space of expected responses to an epoch of stimulation.

The same approach is taken to model the percentage changes in R_2^* and M, with parameters Q_j replaced by R_j and M_j, respectively.

ASL Data at Two Echo Times

Now that we have defined a physiological model of the ASL signal, we can turn our attention to how we model ASL data acquired at multiple echo times. In particular, we will use dual-echo ASL data and ASL data interleaved at two different echo times.

We will denote the perfusion ASL signal at the first echo time as p_{1n} and at the second echo time as p_{2n}, giving two versions of Eq. [1]:

$$p_{1n} = S_n e^{-\mathrm{TE}_1 r_0(1 + r_n/100)}$$
$$p_{2n} = S_n e^{-\mathrm{TE}_2 r_0(1 + r_n/100)}. \quad [9]$$

The measured time series of the ASL data, y_{1n} and y_{2n}, are modeled independently as the sum of these observation/forward models and additive noise terms. This gives

$$y_{cn} = p_{cn} + e_{cn}, \quad [10]$$

where $c = 1$ or $c = 2$ depending on which echo time the data are from. The noise in gradient echo planar imaging data, particularly from the context of BOLD-FMRI, is well understood to contain large components of low-frequency noise or temporal autocorrelation (21). To deal with this we take a similar approach to that which is used in BOLD-FMRI analysis, by removing the worst of the low-frequency noise using high-pass filtering and modeling the remaining noise with a Gaussian autoregressive (AR) model (21),

$$e_{cn} = a_c e_{cn-1} + \epsilon_{cn}$$
$$\epsilon_{cn} \sim N(0, \phi_c^{-1}), \quad [11]$$

with AR parameter a_c and with precision ϕ_c (precision is 1/variance). Note that we assume a different AR and noise variance parameter for the two different echo times. This allows for the possibility that any noise in the system occurring at the level of R_2^* fluctuations will be manifested differently at the two different echo times being used.

Table 1
Free Physiological Parameters in the Model

Parameter	Description
β	$q_0\rho_0^b$, where q_0 is baseline CBF and ρ_0^b is the magnetization per unit volume of arterial blood
Q_j	Percentage change in CBF for basis function j
r_0	Baseline R_2^*
R_j	Percentage change in R_2^* basis function j
M_0	Baseline M, where M is the static magnetization per voxel
M_j	Percentage change in M for basis function j
δt	Transit time delay between tag region and image region

The signal model parameters common to both echo times are summarized in Table 1 and are

$$\boldsymbol{\theta} = \{Q_j, R_j, M_j, r_0, \beta, M_0, \delta t\}, \quad [12]$$

where $\beta = q_0\rho_0^b$, and the echo time specific noise parameters are

$$\boldsymbol{\vartheta_c} = \{a_c, \phi_c\} \quad [13]$$

for $c = 1$ and $c = 2$. Other fixed parameters in the model are given in Table 2.

Bayesian Inference

We have defined a model for predicting ASL data at two different echo times. We now describe how we can use this model to infer the changes in CBF, R_2^*, and M from acquired data. Not only do we want to combine the information from both echo times to estimate the physiological changes, but also we want to be able to characterize our uncertainty in those estimates. Through necessity, our model is nonlinear and multivariate (due to having data at two different echo times). While it may be possible to infer using nonlinear multivariate frequentist statistics, we prefer in this work to use the more amenable framework of Bayesian inference.

The Bayesian framework is the only systematic way to express probabilistic belief in model parameter values given a set of observed data. Bayesian inference has been successfully used previously in MRI to deal with nonlinear BOLD-FMRI models (22,23), and to do probabilistic diffusion-weighted tractography (24).

The two rules at the heart of Bayesian learning techniques are conceptually very simple. The first tells us how (for a model $\mathcal{M}$) we should use the data, $\mathbf{Y}$, to update our *prior* belief in the values of the parameters Θ, $p(\Theta|\mathcal{M})$ to a *posterior* distribution of the parameter values $p(\Theta|\mathbf{Y}, \mathcal{M})$. This is known as Bayes' rule:

$$p(\Theta|\mathbf{Y}, \mathcal{M}) = \frac{p(\mathbf{Y}|\Theta, \mathcal{M})p(\Theta|\mathcal{M})}{p(\mathbf{Y}|\mathcal{M})}. \quad [14]$$

However, this *joint* posterior probability distribution function (PDF) on all parameters, Θ, is often not the distribution that we are most interested in. We are often interested in the posterior *PDF* on a single parameter or an interesting subset of parameters. Obtaining these *marginal* distributions involves performing integrals,

$$p(\Theta_I|\mathbf{Y}, \mathcal{M}) = \int_{\Theta_{-I}} p(\Theta|\mathbf{Y}, \mathcal{M}) d\Theta_{-I} \quad [15]$$

where Θ_I are the parameters of interest and Θ_{-I} are all other parameters. This takes into account the effect our uncertainty on these "nuisance" parameters has on the *PDF*s of the parameters of interest.

Bayesian Inference on ASL Data at Two Echo Times

In this work our data, $\boldsymbol{Y}$, are ASL data acquired at two different echo times, $\boldsymbol{y_1}$ and $\boldsymbol{y_2}$ (i.e., $\boldsymbol{y_c}$ with $c = 1$ and $c = 2$). The parameters $\boldsymbol{\Theta}$ constitute the set of signal model parameters common to both echo times, $\boldsymbol{\theta}$ (Eq. [12]) and the sets of echo time specific noise parameters, $\boldsymbol{\vartheta_1}$ and $\boldsymbol{\vartheta_2}$ (Eq. [13]). The joint posterior over all parameters in Eq. [14] can be written as

$$p(\boldsymbol{\theta}, \boldsymbol{\vartheta_1}, \boldsymbol{\vartheta_2}|\boldsymbol{y_1}, \boldsymbol{y_2}) \propto p(\boldsymbol{y_1}|\boldsymbol{\theta}, \boldsymbol{\vartheta_1})p(\boldsymbol{y_2}|\boldsymbol{\theta}, \boldsymbol{\vartheta_2})p(\boldsymbol{\theta})p(\boldsymbol{\vartheta_1})p(\boldsymbol{\vartheta_2}). \quad [16]$$

The terms $p(\boldsymbol{y_c}|\boldsymbol{\theta}, \boldsymbol{\vartheta_c})$, for $c = 1$ and $c = 2$ represent conditionally independent likelihoods (the probability of the data given the model parameters) for the two separate echo times. These are given by Eqs. [10] and [11].

In using a Bayesian framework we are able (and indeed have) to express our prior belief about the parameters in the model. Here, we use simple Uniform priors, with hard constraints on the range of allowed parameter values, but which otherwise are noninformative. For example, to be consistent with our assumption that all of the tagged bolus of time width TI_1 has entered the imaging region before image acquisition, we assume that $0 < \delta t < TI_2 - TI_1$. See Appendix A for the specification of the priors in our model.

We want to be able to infer the percentage changes in CBF, M, and R_2^* from the data. These percentage changes are represented by the parameters Q_j, R_j, M_j. To obtain the *PDF*s on these parameters of interest we must marginalise out all of the other signal and noise parameters using Eq. [15].

For the nonlinear signal with additive noise models used in this paper, we are able to analytically integrate (marginalize) out the variance parameters, ϕ_c. See Appendix B for the solution to these integrals. However, the integrals for the remaining parameters are not analytic. Hence, for these we

Table 2
Fixed Model Parameters for the Two Different Sequences Used

Parameter	Description	Dual-echo visual data	Interleaved two-echo motor data
TI_1	Time between inversion and tag saturation pulse	0.6 s	0.7 s
TI_2	Time between inversion and image acquisition	1.5 s	1.4 s
α	Inversion efficiency	1.0	1.0
TE_1	Shortest echo time	9.1 ms	23 ms
TE_2	Longest echo time	30 ms	32 ms
T_{1b}	T_1 of delivered arterial blood	1.65 s	1.65 s

use the numerical integration approach of Markov chain Monte Carlo sampling. See Appendix C for how this is implemented.

METHODS

Dual-Echo ASL with Visual Stimulation Experiment

The scans were acquired using a PICORE QUIPSS II pulse sequence on a General Electric Excite 3-T scanner with an eight-channel array coil. Three 8-mm slices were acquired through the primary visual cortex with $TI_1 = 0.6$ s, $TI_2 = 1.5$ s, tag thickness = 10 cm, tag-imaging region gap = 1 cm, FOV 24 cm, flip angle 90°, data matrix size 64×64, and bipolar flow crushing gradients ($b = 2$ s/mm^2). We applied presaturation pulses to the imaging region prior to tagging. Two echos (9.1 and 30 ms) were acquired with spiral readout every TR = 2 s. The stimulus used was a flashing (8 Hz) radial checker board; the first 40 s were rest followed by alternating, 20 s on and 40 s off, repeated four times. We scanned six subjects. Each subject did four runs within a single session. Each run repeated the same paradigm.

ASL Interleaved at Two Echo Times with Graded Motor Stimulation Experiment

The scans are acquired using Q2TIPS on a Siemens 3-T scanner, with $TI_1 = 0.7$ s, $TI_2 = 1.4$ s, tag thickness = 10 cm, tag–imaging region gap = 1.5 cm, FOV 25.6 cm, flip angle 90°, data matrix size 64×64, with bipolar flow crushing gradients. We applied the presaturation pulses to the imaging region prior to the tagging. Two echos (23 and 32 ms) were acquired in an interleaved fashion. Our ability to be able to make use of such data demonstrates the flexibility of the modeling approach proposed. The TR between each measurement is 2.25 s, and the sequence starts tag TE1–tag TE2–control TE1–control TE2 and then repeats. The effective TR between subtracted corresponding tag–control pairs will be 4.5 s. The task is performed by bilateral sequential finger apposition between the thumb and each of the forefingers in the repeated pattern (1) index (2) middle (3) ring (4) little (5) ring (6) middle. Each subject was trained to time the rate of tapping to a flashing cue. Graded activation is achieved by varying the rate of individual finger tapping between approximately 1, 3, 4, and 5 Hz. The experiment begins with 45 s rest followed by alternating 45 s on and 45 s off, repeated over four cycles. The different tapping rates were all performed within a single run. Five different subjects were scanned.

Note that equations we have derived have been for a QUIPSS II sequence and not for Q2TIPS. In QUIPSS II the entire tag region is saturated at time TI_1, whereas in Q2TIPS the leading edge of the tag region is repeatedly saturated from time TI_1 to time TI_3 (the sequence used has $TI_3 = 1.2$ s) after the tag is applied. We can modify the recovery curve for saturated delivered blood when using Q2TIPS to take this difference into account. See Appendix D for details.

Data Processing

The ASL time series have the first four scans removed and then are motion corrected and high-pass filtered using FEAT (25) using a high-pass cut-off of 100 TRs. We then calculated regions of interest (ROIs), which represent spatial areas that have changes relating to brain activation in response to the stimulus. This is achieved by finding areas of strong activation in the ASL data by using a simple pairwise subtraction analysis as follows.

Pairwise subtracted ASL time series are calculated from the data acquired at the shortest echo time and analyzed by fitting a GLM to each voxel's time series using FEAT (25). The regressors in the GLM are formed by convolving the stimulus time course with a simple canonical HRF (Gaussian distribution with mean of 5 s and standard deviation of 2.5 s). To obtain ROIs we threshold the resulting t statistic map at $t = 3$ for the visual datasets and at $t = 2.3$ for the motor datasets. We then calculate the mean time series over the voxels within the ROIs to give the ASL time series, y_1 and y_2. This was done separately for all subjects and runs. Note that a single ROI was determined for all tapping rates in the motor datasets by thresholding on the t statistic map for the fastest tapping rate.

ROI Analysis

For the ROI analysis using Bayesian inference on our proposed nonlinear model, we used a Gaussian basis set to model the percentage R_2^*, CBF, and M temporal changes. This basis set can be seen in Fig. 4a. The basis set contains six basis functions, shifted by different amounts to span the full period between epochs of stimulation. The Gaussian smoothed impulse responses repeat at the same point within each repeated epoch of stimulation, so that they produce time-locked averages of the response across epochs. A standard deviation of 8 s was used for the Gaussian smoothness.

Using a Gaussian basis set incorporates the assumption that the response shapes will be temporally smooth. The actual amount of smoothness imposed will be determined by the number of basis functions and the standard deviation of the Gaussians. These were chosen by qualitatively matching the available CNR to the smoothness imposed.

In the case of the ROI analysis on individual datasets, we found that six basis functions with a standard deviation of 8 s worked well. However, a less smooth basis set was used when the aim was to obtain the average response shapes across all subjects and runs. We can afford less smoothness because we have more data, and therefore a higher CNR. In that case, the basis set used was a Gaussian basis with 15 basis functions and a standard deviation of 2 s. Ideally, the amount of smoothness would be determined from the data itself. This is an area for future work.

Voxelwise Analysis

As well as an ROI analysis, we also perform a *voxelwise* analysis. However, we do not use a basis set as flexible as the Gaussian basis sets from the ROI analysis, as there will be a much lower CNR when working with voxelwise data. Instead we reconstruct response shapes for the percentage R_2^* and CBF changes from an ROI analysis averaged across all subjects and runs using the GLM approach (see next section). These averaged response shapes are shown for the visual dataset in Fig. 5b. The M response shape is taken to be the same as CBF.

Comparison with GLM Approach

We also want to compute percentage *BOLD* and CBF changes using standard linear methods so that we can compare the values we obtain with our Bayesian analysis. Typically, these would be obtained via some form of interpolation and subtraction/addition of the ASL data, before fitting a GLM (16,18). However, Hernandez et al. (17) have recently proposed a method that fits a GLM directly to the ASL data. This has the advantage of using all of the available data, but has the disadvantage of requiring the sort of temporal autocorrelation correction needed in BOLD-FMRI analysis (21). This is the approach we take here.

As with the Bayesian analysis we perform both ROI and voxelwise GLM analyses. The GLM regressors used in the ROI analysis were derived from the same Gaussian basis set used in our Bayesian analysis. Then, as with the Bayesian analysis, we reconstruct response shapes for the BOLD and CBF response shapes from the ROI GLM analysis averaged across all subjects and runs. These averaged response shapes are shown for the visual dataset in Fig. 5b. The resulting regressors used in the voxelwise GLM in the approach of Hernandez et al. (17) are shown in Fig. 2. Note that both the GLM and the Bayesian voxelwise analyses use these same response shapes reconstructed from the GLM ROI analysis. This ensures that any advantage is with the GLM approach when we make comparisons between the GLM approach and our nonlinear Bayesian method using the voxelwise analyses.

We perform temporal autocorrelation correction by using prewhitening using an autoregressive model of order 1 (21). Note that this is the same noise model as we use in the nonlinear Bayesian analysis. This approach is used on both the ROI and the voxelwise data using the same basis sets as the nonlinear Bayesian approach, so that a comparison can be made on the computed percentage BOLD and CBF changes. The GLM analysis was carried out on ASL data at the longest echo time to get percentage BOLD estimates and on ASL data at the shortest echo time to get percentage CBF estimates.

Frequentist t statistics generated from the GLM analysis will relate to probabilities of acquiring the data under the null hypothesis. In contrast, probabilities generated from the Bayesian inference on the nonlinear model will correspond to the belief that we have in a parameter having a particular range of values, given the data. To allow us to compare the statistics from these two different approaches we convert the GLM t statistics into z statistics via a standard probability transform and the Bayesian inference probability density functions into pseudo-z statistics by a probability transform on the probability $P(x > 0)$ from the marginal posterior *PDF* (where, for example, x is percentage change in CBF). For models for which Bayesian inference is analytic and frequentist null hypothesis testing is possible (e.g., the general linear model with Gaussian noise), z statistics and pseudo-z statistics calculated in this way are equivalent (26).

Inferring CBV Changes

In this work we are proposing that we are able to infer percentage changes in R_2^*, CBF, and the static magnetization, M, from dual-echo ASL data. CBF is being directly inferred, and R_2^* relates to blood oxygenation (and blood volume changes) via the BOLD contrast. We now consider what could be causing the changes in the static magnetization, M.

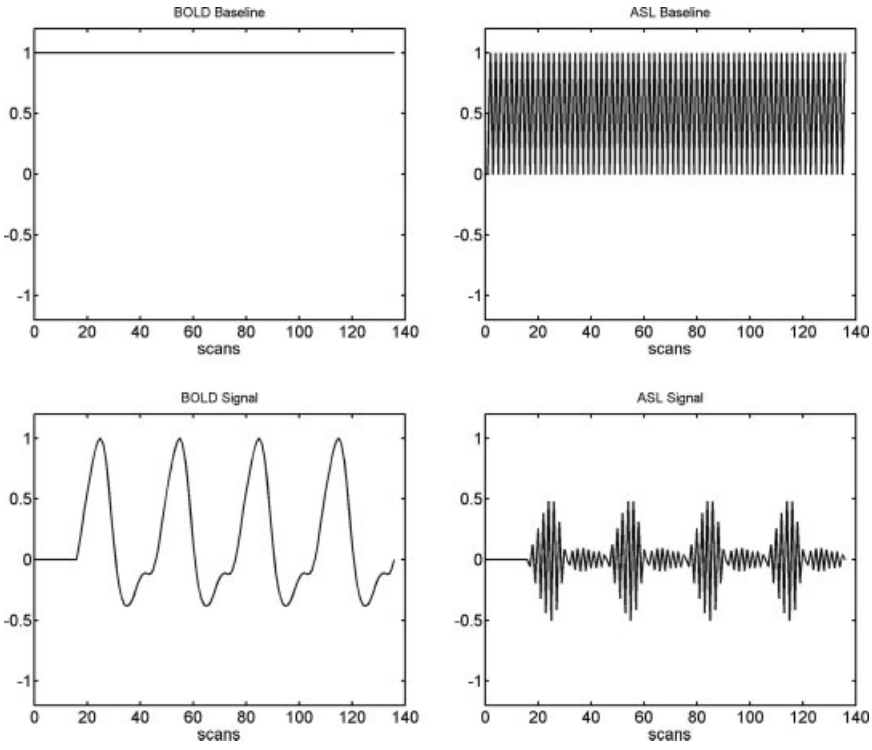

FIG. 2. Regressors used for the voxelwise GLM analysis of the undifferenced ASL data as proposed by Hernandez et al. (17). The response shapes used to obtain the BOLD signal and ASL signal regressors were obtained from a ROI GLM analysis using a Gaussian basis set averaged across all subjects and runs.

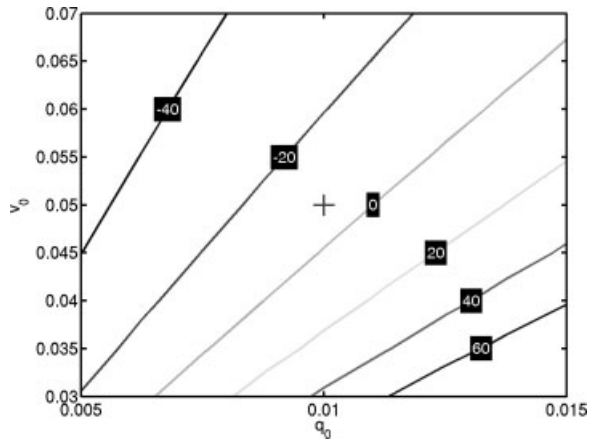

FIG. 3. Plot showing lines of constant percentage error induced in percentage CBV change, i.e., $100 \times (v_{n_{est}} - v_n)/v_n$, by assuming that the static magnetization, M, corresponds to a pure tissue magnetization M_{tissue}. This is calculated using a static compartment model simulation for a range of baseline CBV and baseline CBF values, with parameter values given in Table 3. The cross indicates typical values for baseline CBV and CBF of 5% and 0.01 mL/mL/s, respectively, at which the error is −7.6%

We have defined the contents of the static magnetization as any magnetization that is in the voxel at the time of the tagging pulse and is still within the voxel at the time of image acquistion. We now assume that this includes both static tissue and "static" blood. Note that this does not mean that the blood in question is actually stationary, but that it has not had time to flow out of the voxel between the time of the tagging pulse and the time of image acquistion. For a typical CBF of 0.01 mL/mL/s and baseline CBV of 5%, the mean transit time through the vascular bed of a voxel is 5 s (27). When compared with a time between the tagging pulse and the time of image acquistion of $TI_2 = 1.5$ s, we would not expect the amount of static blood to be negligible. With this in mind we now consider whether it is possible to see how changes in M_n relate to changes in CBV by assuming the same mechanism as in VASO (7).

In VASO (7), the magnetization of the static tissue, M_{tissue}, is measured by approximately nulling blood by using an appropriately tuned inversion recovery. Changes in M_{tissue} can then be related to changes in CBV if a baseline CBV is assumed. An important assumption is that the change in static tissue volume is associated with the exchange of water from the static tissue into the blood. Subsequently, a reduction in static tissue magnetization, M_{tissue}, corresponds to an equivalent percentage reduction in static tissue volume and an increase in blood volume. This can be used to convert a percentage change in the tissue magnetisation, M_{tissue_n}, into a percentage change in CBV, v_n, by assuming a baseline CBV, v_0:

$$v_n = M_{tissue_n}(1 - 1/v_0). \quad [17]$$

In this work, we cannot automatically assume that the changes in the static components magnetization, M_n, inferred in this work corresponds to M_{tissue_n} in VASO. This is because the static magnetization compartment will include contributions from both static tissue and static blood, since we have not nulled the blood signal. To investigate the error in v_n when we assume $M_n = M_{tissue_n}$, we use a model of the blood and tissue components of the static magnetization. This is described in Appendix D. Using this model, specifically via Eq. [33], we can calculate M_n for a given v_n. We can then use this value of M_n in Eq. [17] to calculate an estimate of the percentage CBV, $v_{n_{est}}$, if we assume $M_n = M_{tissue_n}$:

$$v_{n_{est}} = M_n(1 - 1/v_0). \quad [18]$$

We can then calculate the error between $v_{n_{est}}$ and the known v_n.

Figure 3 shows the errors induced in v_n by assuming $M_n = M_{tissue_n}$ for a range of baseline CBF, q_0, and baseline CBV, v_0, values. Table 3 shows the assumed values for the parameters used in Eqs. [33] and [18] to calculate these errors. It can be seen that for typical values of baseline CBF, $q_0 = 0.01$ mL/mL/s, and CBV, $v_0 = 0.05$, the error in v_n when assuming $M_n = M_{tissue_n}$ is only −7.6%.

The reason that this error is small is that $M_{blood_n} \approx 0$, and therefore $M_n \approx M_{tissue_n}$. This is because there are two effects that produce changes in the magnetization in the static blood compartment, and these effects approximately cancel each other out. The first of these effects is an *increase* in magnetization due to water exchange from the static tissue (as assumed in VASO). The second is a *decrease* due to increased blood flow causing less blood to remain in the voxel between the time of the tagging pulse and the time of image acquistion and therefore, by definition, less static blood (recall that static blood is defined as blood that has not had time to flow out of the voxel between the time of the tagging pulse and the time of image acquistion).

However, Fig. 3 also illustrates that the error in v_n by assuming $M_n = M_{tissue_n}$ is sensitive to changes in baseline CBF and baseline CBV. For example, at $q_0 = 0.015$ mL/mL/s and CBV $v_0 = 0.03$ the error has increased to greater than 60%. Furthermore, the error in v_n by assuming $M_n = M_{tissue_n}$ is also sensitive to changes in percentage CBF.

In short, it is *not* in general possible to infer percentage CBV from percentage M changes, since the percentage M changes also depend upon other physiological parameters that are unknown (e.g., baseline CBV, baseline CBF, and percentage CBF changes).

Table 3
Parameters Used in the Static Compartment Model Simulation

Parameter	Description	Value
v_0	Baseline CBV	0.03–0.07
q_0	Baseline CBF	0.005–0.015 mL/mL/s
v_n	Percentage change in CBV	32%
q_n	Percentage change in CBF	100%
r_t	Proton density of gray matter tissue	0.82
r_b	Proton density of blood	0.75
T_{1t}	T_1 of gray matter tissue	1.3 s
T_{1b}	T_1 of blood	1.65 s
TI_2	Time from tag (and image region saturation) to acquisition	1.5 s

Grubb Relationship

In the steady state it has been previously observed that CBV is highly correlated with CBF (28,29). The commonly assumed nonlinear relationship is given by

$$1 + v_n/100 = (1 + q_n/100)^{\alpha}, \qquad [19]$$

where v_n is the percentage change in CBV, q_n is the percentage change in CBF, and α is the Grubb exponent and was measured as being $\alpha \approx 0.4$ by Grubb et al. (28).

Combining Eqs. [18] and [19] gives

$$\alpha = \frac{\log(1 + M_n(1 - 1/v_0)/100)}{\log(1 + q_n/100)}. \qquad [20]$$

Note from the last section that the use of this equation is only valid if we make some strong assumptions about physiological values. However, if we do make those assumptions and we use our inferred percentage changes of static magnetization, M_n, and of CBF, q_n, from the visual and motor datasets in this equation, then we can test whether the estimated Grubb exponents are consistent with those in the literature (28).

RESULTS

ROI Analysis

Figure 5a shows typical model fits to the data from the ROI analysis on an example visual dataset. Also shown are the separate contributions to the fit from the static compartment and delivered blood compartments. Note that these have had their means shifted for ease of display, but are otherwise unscaled, so that their contribution to the variation in the signal can be assessed. Crucially, the good fits in Fig. 5a are achieved simultaneously on the different echo time data using a simple physiological model with only free parameters that are *common* to both echo times. These free parameters are specified in Table 1.

At the shorter echo time the delivered blood compartment contributes most to the signal. However, there is a clear reduction in the signal in the static compartment during periods of activity. In the longer echo time data both compartments contribute considerably to the signal, and both are now clearly being heavily affected by R_2^* effects. Figure 4b shows the inferred *PDF* of the baseline R_2^*. This has mean baseline R_2^* of 25 s^{-1}, corresponding to a baseline T_2^* of 40 ms. The Bayesian inference performed produces *PDF*s for all of the parameters in our model, and it is the means and variances of these distributions that we use to give the mean fits and to perform inference on the parameters.

Figure 4b also shows the inferred *PDF* for the transit time delay, δt. There is a nonzero probability across all of the allowed range. In general the *PDF*s for δt from the ROIs, and also from the voxelwise analyses, were approximately uniform, indicating that there is little or no information available in the data to inform us as to what δt should be. This is because there is no information available to infer the transit time delay from a single inversion time. However, this is not a concern, because this uncertainty in δt is taken into account in the Bayesian framework when we look to infer on the other parameters of interest in our model.

Figure 5b shows the reconstructed average response shapes for the percentage R_2^*, CBF, and M temporal changes from the the ROI analysis averaged across all subjects and runs (six subjects, four runs each). Note that the responses for R_2^* and M have had their signs reversed. This is because neural activity should produce positive changes in CBF, but negative changes in R_2^* and M. The shaded regions show the across subject ($n = 6$ subjects) standard errors (std/sqrt(n)) in the inferred shape. The R_2^* response shows

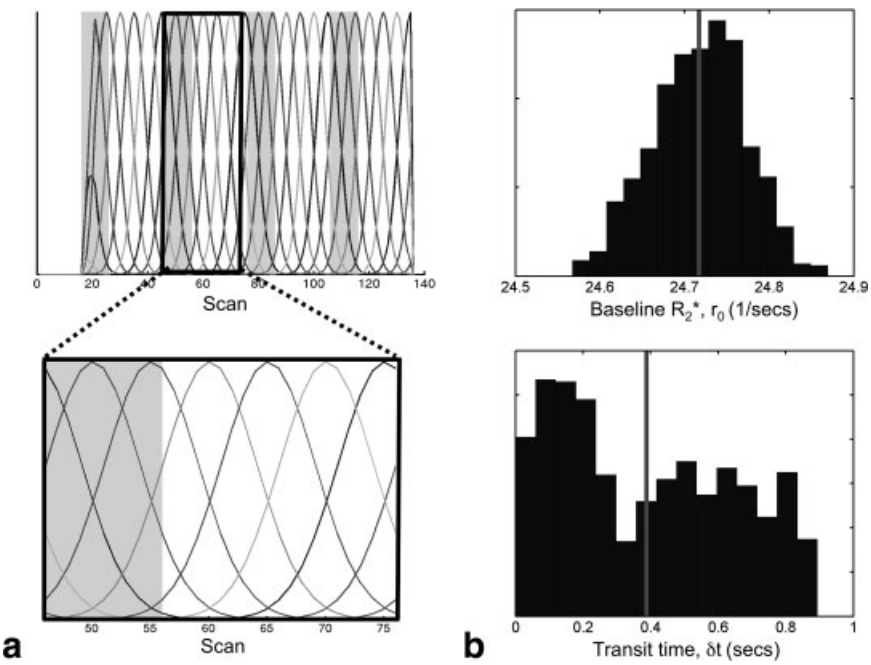

FIG. 4. **(a)** Gaussian basis set used to model the percentage R_2^*, CBF, and M temporal changes in the ROI analysis of the visual dataset. The six different basis functions in the basis set are show on top of each other. The areas of gray correspond to the stimulus being applied. **(b)** The inferred probability density functions (*PDF*) of the baseline R_2^* and the transit delay δt. The Bayesian inference performed produces similar *PDF*s for all of the parameters in our model and can be used to perform inference on the parameters.

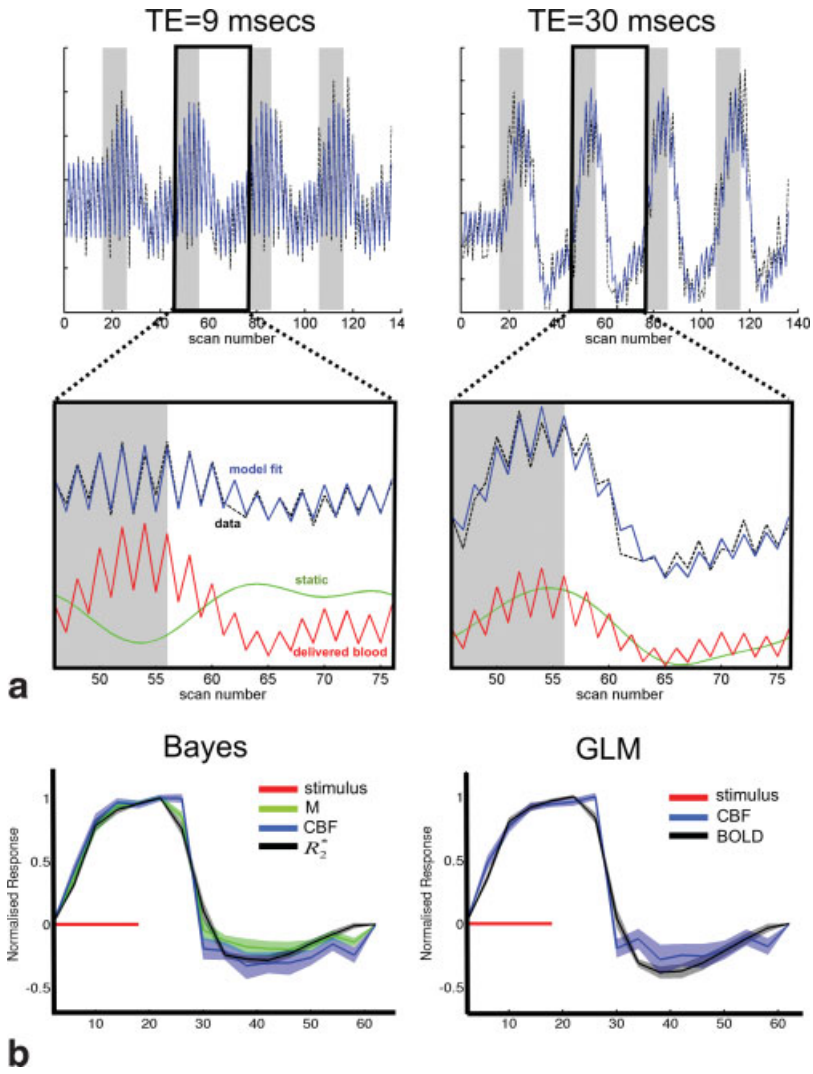

FIG. 5. **(a)** Typical model fits (blue) to the data (black) at the different echo times from the ROI analysis on an example visual dataset. Also shown are the separate contributions to the fit from the static compartment (green) and the delivered blood (red) compartment (note that both also include R_2^* weighting). These have had their means shifted for ease of display, but are unscaled. At the shorter echo time there is a clear reduction in the signal in the static compartment during periods of activity due to the effect of reduced static tissue magnetization. **(b)** Reconstructed response shapes for the percentage R_2^*, CBF, and M temporal changes from the Gaussian basis set fits from the ROI analysis averaged across all subjects and runs for the visual datasets (six subjects, four runs each). The responses have been normalized and the responses for R_2^* and M have had their signs reversed. The shaded regions show the across subject ($n = 6$ subjects) standard errors (std/sqrt(n)) in the inferred shape.

the least variability and suggests the presence of a poststimulus undershoot. Figure 5b also shows the average response shapes for the percentage R_2^* and CBF changes from the GLM analysis for comparison. The responses are qualitatively quite similar, although there appears to be a bigger undershoot for the BOLD/R_2^* response shape in the GLM approach compared to the nonlinear Bayes approach.

Figure 6 shows the comparison of the inferred percentage changes in R_2^*, CBF, and M for the four different graded stimulation strengths in the motor dataset. The inferred percentage changes exhibit a linear trend as the motor stimulation strength increases. Also shown are the inferred mean percentage changes in R_2^*, CBF, and M for each subject from the visual dataset.

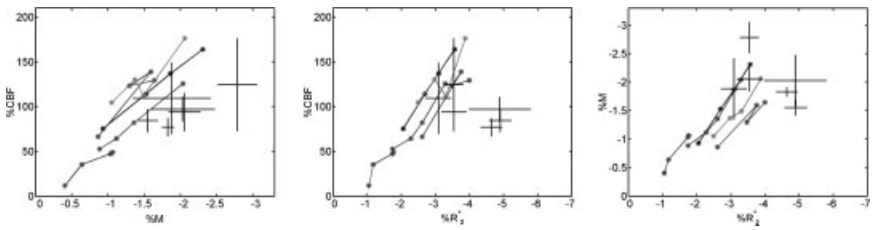

FIG. 6. Comparison of the inferred percentage changes in R_2^*, CBF, and M from the ROI analysis. For each of the five subjects in the motor experiment, the inferred values at the four different motor stimulation strengths are joined by a line in the order of stimulation strength. The percentage changes from the visual dataset ROIs (for which there is a single stimulation strength) are shown as a black cross at each subject's mean. The within-subject, across-run standard deviation is represented by the length of the arms on the crosses (there were four runs per subject).

Voxelwise Analysis

Figure 7 shows the spatial maps of changes in R_2^*, CBF, and M for both example visual and motor datasets. This shows z statistic maps corresponding to the different percentage changes, thresholded at $z = 3$ ($P < 0.005$) alongside the inferred mean percentage changes. All three of R_2^*, CBF, and M show activation within the primary visual cortex (V1) for the visual dataset and within the left and right motor cortex and supplementary motor area (SMA) for the motor datset. The amount of activity inferred is greatest in R_2^*, followed by M and CBF. Figure 8 shows spatial maps of the inferred mean baseline values relating to R_2^*, CBF, and M. The baseline CBF map shows increased CBF in areas of gray matter as would be expected. The baseline M and R_2^* maps are comparatively homogeneous.

In the voxelwise analysis we are assuming a fixed response shape determined from the GLM ROI analysis. However, it is possible that the response shape could vary spatially across the brain, and hence assuming a fixed response shape could result in suboptimal fits. This could be allowed for in the proposed framework by using a basis set of the form commonly used in voxelwise BOLD-FMRI GLM analyses, which includes a canonical HRF, a temporal derivative, and a dispersion derivative (30).

Comparison with GLM Approach

Figures 9 and 10 show comparisons between the GLM analysis and the Bayesian inference on the nonlinear model. Figure 9 shows the z statistic maps corresponding to percentage changes in CBF thresholded at $z = 3$ ($P < 0.005$) for these two techniques for a sample visual dataset. The Bayesian inference approach shows a wider extent of activation in areas of plausible activation.

Figure 10a shows a scatter plot of the unthresholded percentage changes in CBF z statistics and thresholded percentage changes in CBF, comparing the nonlinear Bayesian approach with the GLM approach. The GLM analysis was carried out on ASL data at the shortest echo time. Percentage changes in CBF are similar, but the Bayesian approach shows increased z statistics. These results are consistent with the Bayesian approach being more sensitive than the

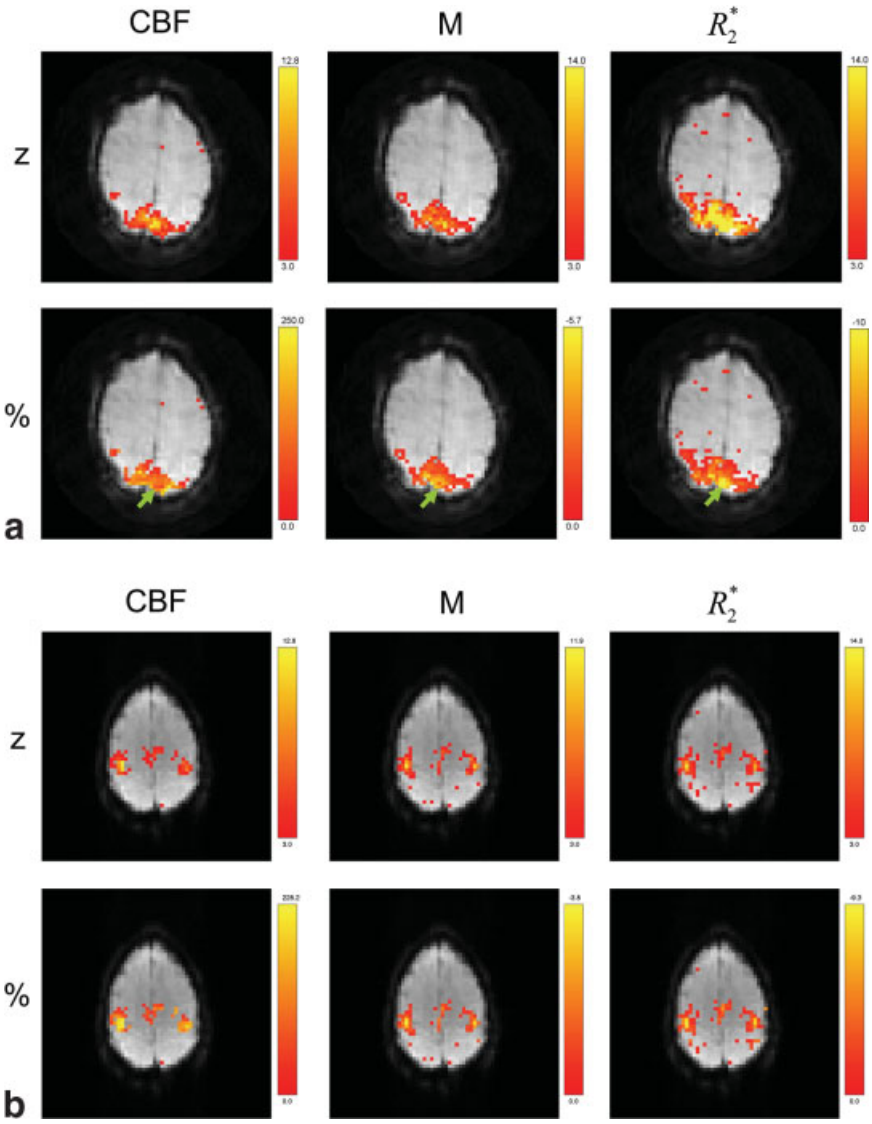

FIG. 7. Spatial maps of changes in R_2^*, CBF, and M for sample datasets. This shows z statistic maps corresponding to the different percentage changes, thresholded at $z = 3$ ($P < 0.005$) alongside the inferred mean percentage changes. **(a)** Sample visual dataset and **(b)** Sample motor dataset. The green arrows on the visual dataset spatial maps indicate the location of a focus of the strongest activation in R_2^*. There is no similar focus of activation in the same location in the spatial maps of CBF and M. This may be due to this area containing the large draining vein of the sagittal sinus, to which R_2^* is sensitive and CBF and M are not.

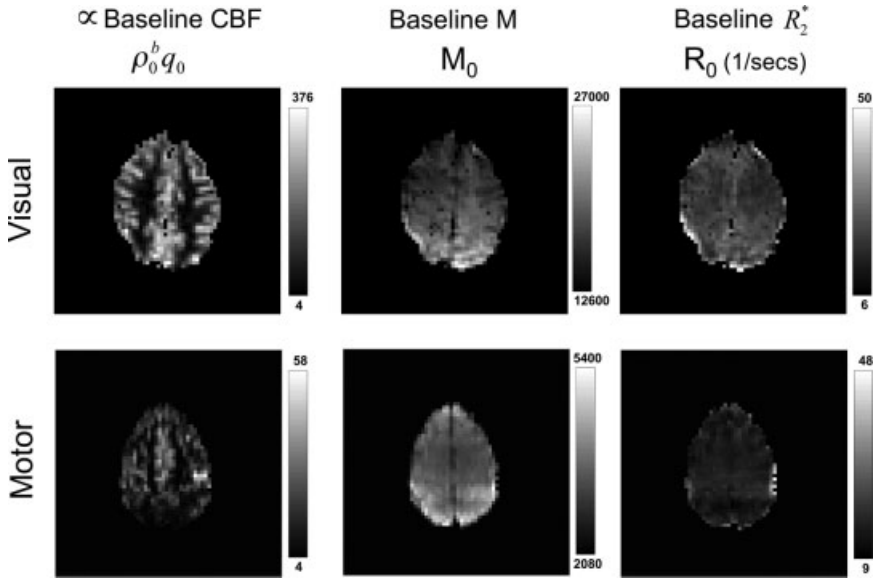

FIG. 8. Spatial maps of inferred mean baselines relating to R_2^*, CBF, and M for (above) sample visual dataset and (below) sample motor dataset. Note that r_0 is in units of s^{-1}, whereas M_0 and $\rho_0^b q_0$ are unitless.

GLM approach for inferring percentage changes in CBF. This is due to the Bayesian inference using all of the available data at both echo times.

Figure 10b shows a scatter plot of the unthresholded percent changes in BOLD z statistics and thresholded percentage changes in BOLD, comparing the nonlinear Bayesian approach with the GLM approach. The GLM analysis was carried out on ASL data at the longest echo time. Percentage changes in BOLD are obtained from the Bayesian approach by using the estimates of baseline and percentage changes in R_2^* and assuming the longest echo time. Percentage changes in BOLD tend to be higher in the Bayesian approach. This is possibly due to the unmodeled static magnetization changes reducing the percentage change in BOLD in the GLM approach.

Noise Parameters

Figure 11 shows the distributions of the AR parameter, a_c, for the different echo times from the ROI analyzes across all runs/subjects from the different datasets. Recall that we are assuming a different AR and noise precision parameter for the two different echo times, as this allows for the possibility that any noise in the system occurring at the level of R_2^* fluctuations will be affected differently at the two different echo times being used. The AR parameters in the visual dataset at the shortest echo time (mean AR(1) of 0.23 at 9 ms) are significantly lower than those at the longest echo time (mean AR(1) of 0.55 at 30 ms) (one-tailed paired t test: $P < 1e-8$).

Although the motor and visual datasets were acquired on different systems, they were both 3-T scanners, and so we might expect the AR coefficients at the 30- and 32-ms echo times to be similar. However, Fig. 11 suggests that this is not the case, with the motor dataset showing much lower autocorrelation. This is because the effective TR between observations at the same echo time in the dual-echo visual data is approximately half that of the interleaved motor data. We would expect the AR(1) coefficient at half the temporal resolution to be a^2. Our inferred autoregressive parameters are consistent with this, with the mean AR(1) coefficient in the visual dataset at approximately 0.5 and that in the motor dataset at approximately 0.25.

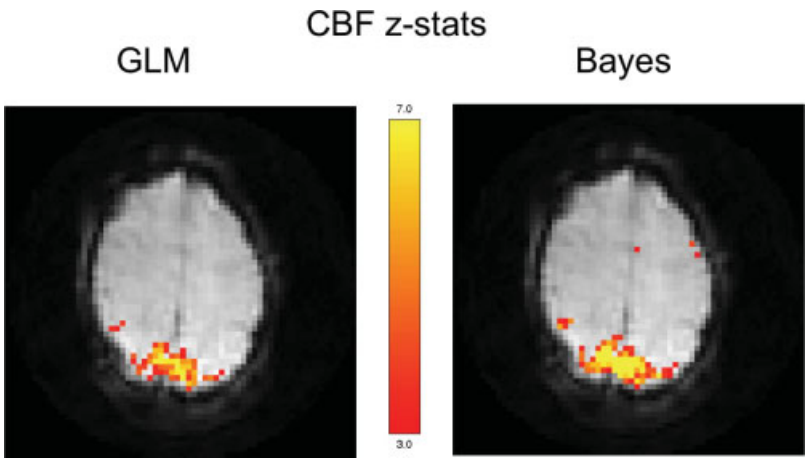

FIG. 9. Comparisons of the nonlinear Bayesian approach with the GLM approach for a voxelwise analysis on an example visual dataset. z statistic maps corresponding to percentage changes in CBF, thresholded at $z = 3$ ($P < 0.005$) for the GLM approach and the Bayesian inference on the nonlinear model approach proposed in this paper, for a sample visual dataset. The Bayesian inference approach shows a wider extent of activation in areas of plausible activation.

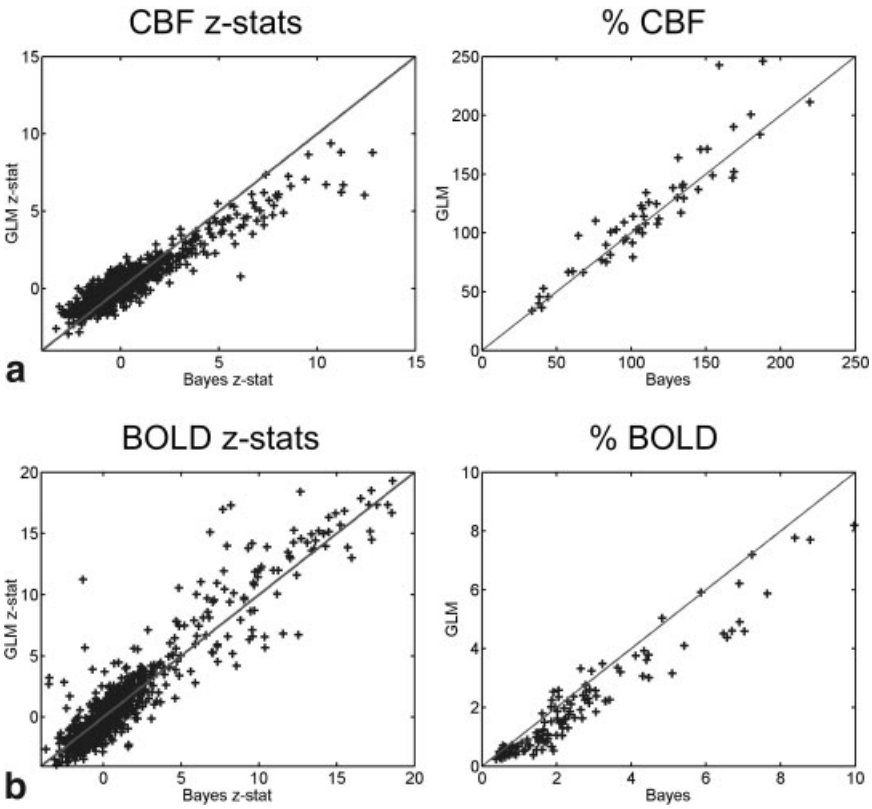

FIG. 10. Comparisons of the nonlinear Bayesian approach with the GLM approach for a voxelwise analysis on a sample visual dataset. **(a)** Scatter plot of the unthresholded percentage changes in CBF *z* statistics and thresholded percentage changes in CBF. Shows increased *z* statistics for the Bayesian approach. **(b)** Scatter plot of the unthresholded percentage changes in BOLD *z* statistics and thresholded percentage changes in BOLD. Shows increased percentage BOLD for the Bayesian approach.

Inferring CBV Changes

Figure 6 shows that we get percentage changes for M from the ROI analyzes in the range -0.5% to -2.5% ($-0.005 < M_n < -0.025$). Using Eq. [18] with a baseline CBV of 5% ($v_0 = 0.05$), this corresponds to percentage changes in CBV from 10 to 48%. We can also use our inferred percentage changes of M and CBF in Eq. [20] to calculate Grubb exponents for assumed baseline CBV values. Figure 12 shows estimates of the Grubb exponent when baseline CBV is fixed to 0.05, for the ROI analyzes across subjects for the visual and motor datasets. The estimated Grubb exponents are consistent with the predicted values of 0.4 from the literature (28). However, note that the inferring CBV and Grubb exponents using the percentage changes in M is based on some strong assumptions about other physiological values (see Inferring CBV Changes).

DISCUSSION

In this work we have proposed a model-based method for extracting information about percentage changes in R_2^*, CBF, and static magnetization, M, from dual-echo ASL data. Being able to simultaneously acquire different quantitative measures may be of importance in studies where it is difficult to reliably reproduce conditions between runs, e.g., gas challenges and drug studies. The explicit modeling of these different contributions to the measured signal provides this complementary information. At the same time, we have shown that this increases sensitivity in inferring CBF changes and reduces contamination in inferring BOLD changes, when compared with linear modeling approaches on single-echo ASL data.

CBF is typically inferred from single-echo ASL data by obtaining a perfusion-weighted time series that consists of

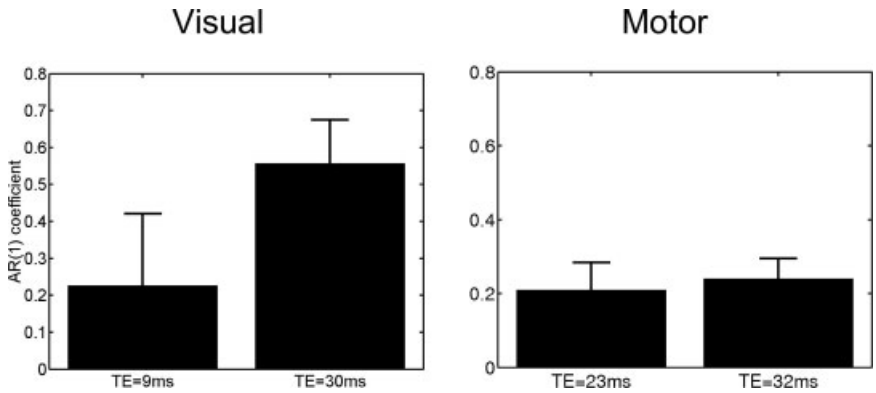

FIG. 11. Distributions of the autoregressive (AR) parameters at the different echo times. The AR parameters in the visual dataset at the shortest echo time are significantly lower than those at the longest echo time.

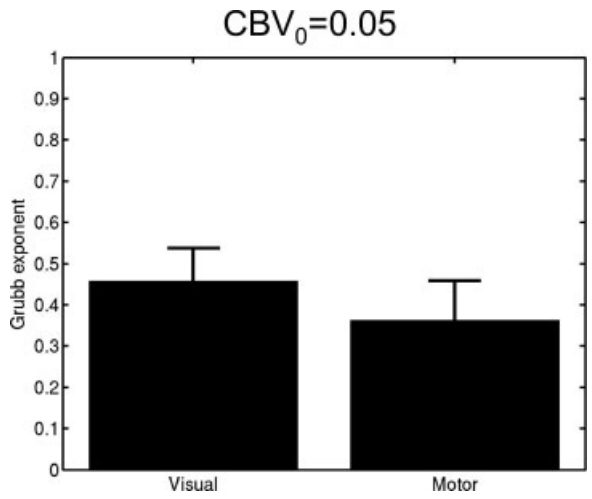

FIG. 12. Distribution of the Grubb exponent when baseline CBV is fixed to 0.05 from the ROI analyzes across subjects for the visual and motor datasets. Note that the error bars correspond to the standard deviation across subjects.

differencing the ASL tag/control pairs (16,18). Changes in BOLD weighting that occur faster than the time between tag and control cause high-frequency contamination of this perfusion-weighted time series. In single-event FMRI experiments the percentage CBF signal will also have signal at high frequencies, and so this contamination is a problem. In this work this problem is avoided because we explicitly model and infer the BOLD changes (and indeed the M changes) alongside the CBF changes, by using all of the information available in dual-echo ASL data.

Static Compartment Contribution to the ASL Signal

The contribution of the static compartment, M, to the ASL signal demonstrated in this work has not (to our knowledge) been previously reported. As demonstrated in Fig. 10b, this component causes fractional changes in BOLD to be underestimated in a standard GLM approach on single-echo ASL data. As illustrated in Fig. 10b, in the GLM approach BOLD changes can be underestimated by around 25%. This has important implications for extracting BOLD changes from ASL data using either averaged tag–control approaches (16), or the more sophisticated available techniques for analyzing single-echo ASL using a linear model (17).

The high z statistics in Figs. 7 and 10 demonstrate that we are able to separate out and infer R_2^*, q_n, and M_n changes from dual-echo ASL data. The reason that we can separate the R_2^* (BOLD) changes from the M (static compartment) changes is that the R_2^* changes are modulated by the two different echo times, whereas the M changes are not. The reason that we can separate the CBF changes from the M changes is that the CBF changes are tag–control modulated, whereas the M changes are not. The nonlinear ASL signal model described in this paper incorporates the contributions to the ASL signal of these different hemodynamic changes, thus allowing them to be inferred from dual-echo ASL data with more accuracy and sensitivity than current GLM approaches on single-echo data. In this work, this inference happens to be achieved with Bayesian inference. However, it is worth noting that it possible that non-Bayesian approaches such as multivariate frequentist statistics could be used to achieve the same results. However, in our experience the Bayesian framework is a more amenable mathematical framework for such nonlinear, multivariate applications.

Sensitivity in Inferring CBF

Figure 10a shows results that are consistent with the proposed method being more sensitive than a GLM approach for inferring percentage changes in CBF. This is despite the fact that we are using one of the more sophisticated available techniques for analyzing ASL using a linear model (17). Figure 5a shows that there is considerable tag–control modulated CBF component in the delivered blood at the longer echo times used as well. The full physiological model allows us to utilize all of the available undifferenced data at both echo times. This provides us with extra information to give us more sensitive estimation of CBF. We note that it is possible that non-Bayesian approaches such as multivariate linear frequentist statistics could be used to combine the data from both echo times to achieve the same sensitivity gains in inferring CBF. However, these techniques would need to be nonlinear if R_2^* and M changes were to be inferred as well.

Model Validity

The results found in this work appear to be biophysically plausible (e.g., Figs. 5, 6, 7, and 12), and we obtain good model fits to data acquired at both echo times (e.g., Fig. 5a). Plausible physiological results were obtained across runs/subjects, between the motor and visual region, and between two different sequences (either with dual-echoes from a single shot or two different echo times interleaved). This is encouraging validation of the model assumptions within the context of inferring the relevant physiological changes from this kind of data.

The model is intended to be as simple as possible, while still describing the primary components of variation in the measured signal in ASL data.

We assume no exchange between the static tissue compartment and the delivered blood, and we assume no clearance of this delivered blood due to outflow. These two effects result in the factor q in Buxton (19) and Wong (9), and are considered small, resulting in a value for the factor q close to unity. If the time of exchange is approximately 1 s after the delivered blood has arrived in the voxel, then with $TI_2 = 1.5$ s (27) the majority of the longitudinal relaxation will occur in the blood. So, the effects of exchange between the static tissue compartment and the delivered blood should be small. For a CBF of 0.01 mL/mL/s and baseline CBV of 5%, the mean transit time through the vascular bed of a voxel is 5 s, compared to our $TI_2 = 1.5$ s (27). Subsequently, little or no venous outflow of the delivered blood would be expected.

We are also assuming that the transit time δt is the same between activation and baseline. However, we expect that the inference of CBF is driven by signal change between tag and control, for which QUIPSS II is designed to be less

sensitive to changes in δt. Therefore, we would not expect the systematic overestimation of CBF, which is possible in other techniques due to shortened δt with activation (9). Further work is required to verify this.

VASO and CBV

In VASO, changes in tissue magnetization, M_{tissue}, are obtained by assuming that all blood is nulled. By contrast, in this work we obtain changes in the static compartment (blood and tissue which is in the voxel at the time of tagging, and remains there at the time of image acquisition), M, by modeling out the contribution of the delivered blood to the measured signal. As investigated under Inferring CBV Changes, M and M_{tissue} are only equivalent if we neglect the signal from static blood. We showed using simulations from a model of the static tissue and static blood compartments that the contribution from the static blood is small for typical values of baseline CBV (5%) and CBF (0.01 mL/mL/s) (Fig. 3).

However, Fig. 3 also illustrated that the error induced in v_n by assuming $M_n = M_{tissue_n}$ is sensitive to changes in baseline CBF and baseline CBV. For example, at $q_0 = 0.015$ mL/mL/s and CBV $v_0 = 0.03$ the error has increased to greater than 60%. This means that this method can not be used as a general approach for inferring CBV changes, as baseline shifts of this magnitude are to be expected. In future work we intend to address this by incorporating the model of the static tissue and static blood compartments into the Bayesian inference. We would predict that this could prove particularly powerful when combined with alternative acquisition schemes such as the combined ASL, VASO, and BOLD imaging technique of Yang et al. (8).

Noise Modeling

In our model we are assuming a different AR and noise precision parameter for the two different echo times. This allows for the possibility that any noise in the system occurring at the level of R_2^* fluctuations will manifest differently at the two different echo times being used. We show in Fig. 11 that the AR parameters in the visual dataset at the shortest echo time (9 ms) are significantly lower than those at the longest echo time (30 ms). This suggests the possibility that there is temporally correlated noise specific to R_2^*, which is likely to be physiological in origin. In future, instead of having two different sets of noise parameters, it should be possible to link the correlations between echo times by modeling the noise at the level of fluctuations in R_2^*. Similarly, noise could be modeled at the level of CBF and M fluctuations to help us better understand the different contributions to the overall noise in the data.

On a 2-GHz Intel PC the technique takes approximately 30 min on a single slice of the visual data. Future work will be done on alternative inference techniques to MCMC, which should speed up the inference considerably. For example, approximate Bayesian inference approaches such as Laplace or variational Bayes could be used and are orders of magnitude faster (31).

CONCLUSIONS

In this work an approach has been developed that provides simultaneous inference on hemodynamic changes via a nonlinear physiological model of dual-echo ASL data. Importantly, this includes a significant contribution by changes in the static magnetization, M, to the ASL signal. The required multivariate, nonlinear inference is carried out using a Bayesian framework. This approach is able to extract probabilistic estimates of percentage changes of CBF, R_2^*, and the static magnetization, M, and provides increased sensitivity in inferring CBF changes and reduced contamination in inferring BOLD changes when compared with linear modeling approaches on single-echo ASL data.

APPENDIX A

Priors

In using a Bayesian framework we are able (and indeed have) to express our prior belief about the parameters in the model. We use simple Uniform priors, with hard constraints on the range of allowed parameter values but otherwise noninformative. For the percentage changes in CBF, R_2^*, and M we limit the ranges to

$$p(Q_j) \sim \text{Uniform}(-1000\%, 1000\%),$$
$$p(R_j) \sim \text{Uniform}(-1000\%, 1000\%)$$
$$p(M_j) \sim \text{Uniform}(-1000\%, 1000\%) \quad [21]$$

and where Uniform (lower, upper) indicates a Uniform distribution between lower and upper and zero probability outside. The upper and lower limits correspond to the fact that we do not expect changes in CBF, R_2^*, or M greater than $\pm 1000\%$. This is to constrain the model inference to plausible physiological values. On the visual and motor datasets used in this work, we found that we obtain the same results with or without these limits.

The transit time delay, δt, is the time between when the blood leaves the tag region and when it arrives in the imaging region. To be consistent with our assumption in using QUIPSS II that all of the tagged bolus of time width TI_1 has entered the imaging region before image acquisition, we assume that $0 < \delta t < \text{TI}_2 - \text{TI}_1$. The prior is otherwise noninformative:

$$p(\delta t) \sim \text{Uniform}(0, \text{TI}_2 - \text{TI}_1). \quad [22]$$

The remaining signal model parameters, r_0, β, M_0, just require positivity constraints but are otherwise noninformative:

$$p(q_0) \sim \text{Uniform}(0, \infty), \quad p(r_0) \sim \text{Uniform}(0, \infty),$$
$$p(M_0) \sim \text{Uniform}(0, \infty). \quad [23]$$

For the noise parameters we use a non informative reference prior for the variance parameters and a noninformative uniform prior for the autoregressive parameters:

$$p(\phi_c) = 1/\phi_c, \quad p(a_c) = \text{Uniform}(-1, 1). \quad [24]$$

APPENDIX B

Analytic Marginalization of the Noise Variance Parameters

We can perform the marginalization integrals in Eq. [15] for the noise variance parameters, ϕ_c, analytically:

$$p(\boldsymbol{\theta}, a_1, a_2|\boldsymbol{y_1}, \boldsymbol{y_2}) = \int_{-\infty}^{\infty}\int_{-\infty}^{\infty} p(\boldsymbol{\theta}, \boldsymbol{\vartheta_1}, \boldsymbol{\vartheta_2}|\boldsymbol{y_1}, \boldsymbol{y_2}) d\phi_1 d\phi_2. \quad [25]$$

Inserting Eq. [16] and using the priors from Appendix A this can be shown to give

$$p(\boldsymbol{\theta}, a_1, a_2|\boldsymbol{y_1}, \boldsymbol{y_2}) = p(\boldsymbol{\theta})p(a_1)p(a_2)\int_{-\infty}^{\infty} p(\boldsymbol{y_1}|\boldsymbol{\theta}, \boldsymbol{\phi_1})p(\phi_1)d\phi_1 \times \int_{-\infty}^{\infty} p(\boldsymbol{y_2}|\boldsymbol{\theta}, \boldsymbol{\vartheta_2})p(\phi_2)d\phi_2, \quad [26]$$

where

$$\int_{-\infty}^{\infty} p(\boldsymbol{y_c}|\boldsymbol{\theta}, \boldsymbol{\phi_c})p(\phi_c)d\phi_c = \left[\sum_n (e_{cn} - a_c e_{cn-1})^2\right]^{-N/2}, \quad [27]$$

where $e_{cn} = y_{cn} - p_{cn}$, and the priors are given in Appendix A.

APPENDIX C

Markov Chain Monte Carlo Sampling

We can perform the marginalization integrals in Eq. [15] for the autoregression parameters and signal parameters by drawing samples in parameter space from the joint posterior distribution. This implicitly performs the integrals numerically. Markov Chain Monte Carlo (MCMC) (see Gilks (32) for a text on MCMC) is a sampling technique that addresses this problem by proposing samples preferentially in areas of high probability. This allows for many samples to be drawn and, in many cases, for the posterior *PDF* to be built in a *relatively* short period of time.

We use single-component Metropolis–Hastings jumps (i.e., we propose separate jumps for each of the parameters in turn) for all parameters. We use separate Normal proposal distributions for each parameter, with the mean fixed on the current value, and with a scale parameter σ_i for the *ith* parameter that is updated every 30 jumps. At the ℓth update σ_i is updated according to

$$\sigma_i^{\ell+1} = \sigma_i^{\ell}\mathcal{S}\frac{(1 + \mathcal{A} + R)}{(1 + \mathcal{R})}, \quad [28]$$

where $\mathcal{A}$ and $\mathcal{R}$ are the number of accepted and rejected jumps since the last σ_i update, respectively, $\mathcal{S}$ is the desired rejection rate, which we fix at 0.5. A burn-in of 5000 jumps is used (this ensures convergence such that the subsequent samples are from the true PDF), followed by a further 5000 jumps, with the result of every 10*th* jump stored as a sample from the PDF.

APPENDIX D

Saturated Blood Signal in Q2TIPS

In QUIPSS II the entire tag region is saturated at time TI_1, whereas in Q2TIPS the leading edge of the tag region is effectively repeatedly saturated from time TI_1 to time TI_3 after the tag is applied. We can modify the QUIPSS II saturated blood term in Eqs. [4] and [5],

$$\rho_0^b q_0(1 + q_n/100)(\mathrm{TI}_2 - \mathrm{TI}_1 - \delta t)(1 - e^{-(\mathrm{TI}_2 - \mathrm{TI}_1)/T_{1b}}) \quad [29]$$

when using Q2TIPS to take this difference into account.

With Q2TIPS we can say that saturated blood arriving at time t after the tag is applied ($\delta t + \mathrm{TI}_1 < t < \mathrm{TI}_2$) will have received the saturation pulse at approximately time $t - \delta t$. Therefore, the saturated blood magnetization that has arrived in the voxel at time $t = \mathrm{TI}_2$ in tag or control is

$$\rho_0^b q_0(1 + q_n/100)\int_{\delta t + \mathrm{TI}_1}^{\mathrm{TI}_2}(1 - e^{-(\mathrm{TI}_2 - (t - \delta t)/T_{1b})})dt = \rho_0^b q_0(1 + q_n/100)\big((\mathrm{TI}_2 - \mathrm{TI}_1 - \delta t) + T_{1b}e^{-(\mathrm{TI}_2 - \mathrm{TI}_1)/T_{1b}} - T_{1b}e^{-\delta t/T_{1b}}\big). \quad [30]$$

APPENDIX E

Static Compartment Model

We assume that the delivered arterial blood replaces the static blood and that VASO water exchange is reflected in changes in the volume of the static blood compartment. Subsequently, the static blood signal, y_b, consists of blood that has been replaced by delivered blood plus changes in volume due to VASO water exchange,

$$y_b = (v_0(1 + v_n/100) - q_0(1 + q_n/100)\mathrm{TI}_2)s_b r_b K, \quad [31]$$

where $s_b = (1 - exp(-\mathrm{TI}_2/T_{1b}))$, r_b is the proton density of blood, and K is a constant that converts proton density into the MR signal. Similarly, the static blood signal, y_t, consists of changes in volume due to VASO water exchange,

$$y_t = (1 - v_0(1 + v_n/100))s_t r_t K, \quad [32]$$

where $s_t = (1 - exp(-\mathrm{TI}_2/T_{1t}))$, and r_t is the proton density of gray matter tissue. We can now calculate the overall percentage change in the static compartment as

$$M_n = 100\frac{(v_0 v_n/100 - q_0 q_n \mathrm{TI}_2/100)s_b r_b - v_0 v_n s_t r_t/100}{(v_0 - q_0\mathrm{TI}_2)s_b r_b + (1 - v_0)s_t r_t}. \quad [33]$$

REFERENCES

1. Ogawa S, Lee TM, Nayak AS, Glynn P. Oxygenation-sensitive contrast in magnetic resonance image of rodent brain at high magnetic fields. Magn Reson Med 1990;14:68–78.
2. Kwong K, Belliveau J, Chesler D, Goldberg I, Weisskoff R, Poncelet B, Kennedy D, Hoppel B, Cohen M. Dynamic magnetic resonance imaging of human brain activity during primary sensory stimulation. Proc Natl Acad Sci USA 1992;89:5675–5679.
3. Turner R, Le Bihan D, Moonen CT, Despres D, Frank J. Echo-planar time course MRI of cat brain oxygenation changes. Magn Reson Med 1991;22:159–166.

4. van Zijl PC, Ulug AM, Eleff SM, Ulatowski JA, Traystman RJ, Oja JM, Kauppinen RA. Quantitative assessment of blood flow, blood volume and blood oxygenation effects in functional magnetic resonance imaging. Duodecim 1998;114:808–809.
5. Williams DS, Detre JA, Leigh JS, Koretsky AP. Magnetic resonance imaging of perfusion using spin inversion of arterial water. Proc Natl Acad Sci USA 1992;89:212–216.
6. Detre J, Leigh J, Williams D, Koretsky A. Perfusion imaging. Magn Reson Med 1992;23:37–45.
7. Lu H, Golay X, Pekar J, van Zijl P. Functional magnetic resonance imaging based on changes in vascular space occupancy. Magn Reson Med 2003;50:263–274.
8. Yang Y, Gu H, Stein EA. Simultaneous MRI acquisition of blood volume, blood flow, and blood oxygenation information during brain activation. Magn Reson Med 2004;52:1407–1417.
9. Wong E, Buxton R, Frank L. Quantitative imaging of perfusion using a single subtraction (QUIPSS and QUIPSS II). Magn Reson Med 1998;39:702–708.
10. Buxton R, Wong E, Frank L. Dynamics of blood flow and oxygenation changes during brain activation: the balloon model. Magn Reson Med 1998;39:855–864.
11. Hoge R, Atkinson J, Gill B, Crelier G, Marrett S, Pike G. Investigation of bold signal dependence on cerebral blood flow and oxygen consumption: the deoxyhemoglobin dilution model. Magn Reson Med 1999;42:849–863.
12. Posse S, Wiese S, Gembris D, Mathiak K, Kessler C, Grosse-Ruyken ML, Elghahwagi B, Richards T, Dager SR, Kiselev VG. Enhancement of BOLD-contrast sensitivity by single-shot multi-echo functional MR imaging. Magn Reson Med 1999;42:87–97.
13. Silva AC, Lee SP, Yang G, Iadecola C, Kim SG. Simultaneous blood oxygenation level-dependent and cerebral blood flow functional magnetic resonance imaging during forepaw stimulation in the rat. J Cereb Blood Flow Metab 1999;19:871–879.
14. Luh WM, Wong EC, Bandettini PA, Ward BD, Hyde JS. Comparison of simultaneously measured perfusion and BOLD signal increases during brain activation with T(1)-based tissue identification. Magn Reson Med 2000;44:137–143.
15. Schulte AC, Speck O, Oesterle C, Hennig J. Separation and quantification of perfusion and BOLD effects by simultaneous acquisition of functional $I(0)$- and $T2(*)$-parameter maps. Magn Reson Med 2001;45:811–816.
16. Aguirre G, Detre J, Zarahn E, Alsop D. Experimental design and the relative sensitivity of bold and perfusion FMRI. NeuroImage 2002; 15:488–500.
17. Hernandez-Garcia L, Lee G, Mumford J, Nichols T. Estimation efficiency and statistical power in arterial spin labeling FMRI. Int Soc Magn Reson Med 2005;13:1579.
18. Liu TT, Wong EC. A signal processing model for arterial spin labeling functional MRI. NeuroImage 2005;24:207–215.
19. Buxton R, Frank L, Wong E, Siewert B, Warach S, Edelman R. A general kinetic model for quantitative perfusion imaging with arterial spin labelling. Magn Reson Med 1998;40:383–396.
20. Josephs O, Turner R, Friston K. Event-related FMRI. Hum Brain Mapp 1997;5:1–7.
21. Woolrich M, Ripley B, Brady J, Smith S. Temporal autocorrelation in univariate linear modelling of FMRI data. NeuroImage 2001;14:1370–1386.
22. Friston KJ. Bayesian estimation of dynamical systems: an application to FMRI. NeuroImage 2002;16:513–530.
23. Woolrich M, Jenkinson M, Brady J, Smith S. Fully Bayesian spatio-temporal modelling of FMRI data. IEEE Trans Med Imaging 2004;23: 213–231.
24. Behrens T, Woolrich M, Jenkinson M, Johansen-Berg H, Nunes R, Clare S, Matthews P, Brady J, Smith S. Characterisation and propagation of uncertainty in diffusion weighted MR imaging. Magn Reson Med 2003;50:1077–1088.
25. FSL. http://www.fmrib.ox.ac.uk/fsl.
26. Lee P. Bayesian statistics. Arnold; London, UK: 1997.
27. Buxton RB. Quantifying CBF with arterial spin labeling. J Magn Reson Imaging 2005;22:723–726.
28. Grubb R, Phelps M, Eichling J. The effects of vascular changes in $PaCO_2$ on cerebral blood volume, blood flow and vascular mean transit time. Stroke 1974;5:630–639.
29. Mandeville J, Marota J, Kosofsky B, Keltner J, Weissleder R, Rosen B, Weisskoff RM. Dynamic functional imaging of relative cerebral blood volume during rat forepaw stimulation. Magn Reson Med 1998;39: 615–624.
30. Woolrich M, Behrens T, Smith S. Constrained linear basis sets for HRF modelling using variational Bayes. NeuroImage 2004;21:1748–1761.
31. Penny W, Kiebel S, Friston K. Variational Bayesian inference for FMRI time series. NeuroImage 2003;19:1477–1491.
32. Gilks W, Richardson S, Spiegalhalter D. Markov chain Monte Carlo in practice. Chapman and Hall; London: 1996.